

Observation and modelling of atmospheric OH and HO₂* radicals at a subtropical rural site and implications for secondary pollutants

Zhouxing Zou^{1#}, Tianshu Chen^{1#}, Qianjie Chen¹, Weihang Sun¹, Shichun Han¹, Zhuoyue Ren², Xinyi Li², Wei Song², Aoqi Ge², Qi Wang², Xiao Tian², Chenglei Pei³, Xinming Wang², Yanli Zhang², and Tao Wang¹

[#] These authors contributed equally to this work

¹ Department of Civil and Environmental Engineering, The Hong Kong Polytechnic University, Hong Kong, China

² Guangzhou Institute of Geochemistry, Chinese Academy of Sciences, Guangzhou, China

³ Guangdong Province Guangzhou Ecological Environment Monitoring Center Station, Guangzhou 510030, China.

Correspondence to: Tao Wang (tao.wang@polyu.edu.hk)

Abstract

HO_x radicals (OH and HO₂) are crucial oxidants that determine atmospheric oxidation capacity and the production of secondary pollutants; however, their sources and sinks remain incompletely understood in certain rural, forest and maritime environments. This study measured HO₂* (HO₂ + contribution from RO₂, organic peroxy radicals) and OH concentrations using a chemical ionisation mass spectrometer at a subtropical rural site in southern China from 12 November to 19 December 2022. The average peak concentrations were $3.50 \pm 2.47 \times 10^6 \text{ cm}^{-3}$ for OH and $1.34 \pm 0.93 \times 10^8 \text{ cm}^{-3}$ for HO₂*. Model estimated contribution from RO₂ to HO₂ during the measurement period ranged from 44% to 69% of the HO₂*. Calculations based on an observation-constrained chemical model revealed an overestimation of HO₂ and OH concentrations during warm periods of the field study. Sensitivity tests suggest that adding HO_x sinks or a HO₂ recycle process to the model could improve the model performance. Over-simulation of HO_x in the model resulted in overestimations of midday production rates by more than 79% for ozone and a factor of 1.88 for nitric acid. Our study highlights

the need for further improving understanding of the sources/sinks of OH and HO₂ and representation of them in air quality models.

1. Introduction

The HO_x family, comprising hydroxyl (OH) and peroxy radicals (HO₂), plays a pivotal role in the Earth's atmosphere by driving photochemical processes that influence the air composition and chemistry. OH radicals are primarily produced by the photolysis of ozone (O₃), nitrous acid (HONO), and ozonolysis of alkenes. They initiate the oxidation of CO and most volatile organic compounds (VOCs), producing HO₂ and other organic peroxy radicals (RO₂, where R represents an organic group such as alkyl, acyl, or aryl). HO₂ is also generated from the photolysis of oxygenated VOCs (OVOCs) and by reactions between OVOCs and OH. In the presence of NO, RO₂ radicals are converted to HO₂ and then to OH radicals, buffering OH concentrations and maintaining atmospheric oxidation capacity. (Stone et al., 2012). These interactions are crucial in the formation of photochemical smog and secondary organic aerosol (SOA), which generate NO₂, O₃, and highly oxygenated molecules. HO_x (OH + HO₂) radicals are removed through reactions of OH with inorganic trace gases, self-reactions among radicals, peroxyacetyl nitrate (PAN) formation, and the heterogeneous uptake by aerosols. These processes subsequently contribute to atmospheric acidification and aerosol formation through the production of H₂SO₄ and HNO₃. See Figure S1 and Table S1 for detailed processes and chemical reactions.

The accuracy of model-predicted OH is a crucial indicator for assessing our understanding of atmosphere processes (Heard and Pilling, 2003). There is a longstanding debate regarding the discrepancies between simulated and observed radical concentrations under low NO_x conditions, which remains a significant issue (Hofzumahaus et al., 2009; Stone et al., 2012; Zou et al., 2023). Previous studies have shown that models generally predict OH levels well in polluted conditions (NO > 1 ppb), but notable overestimations were observed under low NO and aged conditions, such as coastal areas (Kanaya et al., 2007; Zou et al., 2023), marine boundary layers (Berresheim et al., 2002; Carslaw et al., 1999), and the rural area (Bottorff et al., 2023;

Kanaya et al., 2012). Missing OH sinks from both measurement and chemical mechanism were proposed as the primary reason for the overestimation (Lou et al., 2010; Yang et al., 2016; Hansen et al., 2014; Thames et al., 2020). Underestimations of OH concentrations were also observed in high biogenic VOCs (BVOCs) and low NO (<1 ppb) conditions which generally happen in the subtropical or tropical area (Hofzumahaus et al., 2009; Lelieveld et al., 2008; Tan et al., 2001; Whalley et al., 2011). After considering a new OH regeneration mechanism (Wennberg et al., 2018; Novelli et al., 2020) and measurement interference (Feiner et al., 2016; Hens et al., 2014; Mao et al., 2012; Novelli et al., 2014; Woodward-Massey et al., 2020), daytime OH concentrations could be reasonably reproduced by the model in the high BVOC conditions, with some unresolved underestimation in the evening (Jeong et al., 2022; Lew et al., 2020; Tan et al., 2019). Those results call for more measurement and modelling in subtropical and tropical rural areas.

HO₂ concentrations were consistently underpredicted in the polluted urban sites (Ma et al., 2019; Yang et al., 2021; Ma et al., 2022), with no clear trends in relatively clean regions. Some studies reported good agreement between measurement and model prediction (Feiner et al., 2016; Lew et al., 2020), whereas others indicated model overprediction (Bottorff et al., 2023; Griffith et al., 2013) and underprediction (Whalley et al., 2010; Kim et al., 2013; Mallik et al., 2018; Tan et al., 2017;). These discrepancies may be attributed to several factors, including measurement interference caused by RO₂ recycling in environments rich in BVOCs or aromatics (Fuchs et al., 2011), uncertainties associated with heterogeneous uptake in box models (Yang et al., 2022), and the outflow (or entrainment) of reservoir species like PAN (Griffith et al., 2013) (Whalley et al., 2010). Despite these advances, it remains difficult to pin down the exact causes of the model-measurement discrepancies in some of the previous studies.

In the present study, we measured concentrations of OH and HO₂* (HO₂ + contribution from RO₂) using a quadrupole chemical ionization mass spectrometer (PolyU-CIMS) from November to December 2022 at a subtropical rural site in southern China. We tested model's capability in reproducing the radical concentrations and

elucidate factors contributing to discrepancy under varying temperatures, VOCs, and NO_x conditions. The Methodology section describes the measurement site, the principles and the configuration of PolyU-CIMS, and the setup of chemical box models. The Results and Discussion section details our findings, providing an analysis of the radical concentrations and exploring the discrepancies between observed data and model predictions. By employing an observation-constrained box model, we analyzed the radical budgets and investigated potential causes for these discrepancies. The study concludes with a discussion of the implications of these findings.

2. Methodology

2.1 Measurement Site

The field campaign was conducted at the Conghua Liangkou Air Monitoring Station (23°44'47"N, 113°47'06"E, 200m, above sea level) from November 12 to December 19, 2022 (Figure 1). The site is located at the northern part of the Pearl River Delta (PRD), approximately 80 kilometers from the densely populated areas. It is nestled within the Liuxi River National Forest Park (an evergreen broad-leaf forest). The site is situated just north of the G105 national highway and around 0.5 kilometers east of Liangkou town. Even though it is close to the road, the traffic was generally limited during the observation period due to the coronavirus disease pandemic (COVID-19). The site is subject to BVOCs emission, predominantly isoprene, from the surrounding forest when the daytime temperatures exceeds 20°C, and NO emissions from the nearby national highway, particularly during periods of low wind speeds. The measurements included trace gases such as O₃, NO, NO₂, CO, HONO, VOCs, OVOCs, meteorological data such as relative humidity (RH), temperature, and photolysis frequencies of HONO, NO₂, O₃, H₂O₂, and HCHO. Details about the instruments are shown in Table S2.



Figure 1 Geographic location of the measurement site (Liangkou Air Monitoring station 23°44'47"N, 113°47'06"E, 200 m a.s.l. marked by the red inverted triangle) in Conghua, Guangdong Province, South China. The map is sourced from © Google Earth and © Amap.

2.2 Radical measurement principle

OH and HO₂^{*} radicals were measured using the Hong Kong Polytechnic University's quadrupole Chemical Ionization Mass Spectrometer (PolyU-CIMS), which had been used in a previous study for OH measurement (Zou et al., 2023). The use of CIMS for OH measurement was pioneered by Eisele and Tanner (1991), with subsequent enhancements in measurement accuracy (Eisele and Tanner, 1993; Tanner et al., 1997; Tanner and Eisele, 1995) and the adoption of inlets for simultaneous measurements of HO₂ and RO₂ (Edwards et al., 2003; Sjostedt et al., 2007), H₂SO₄ (Mauldin III et al., 2004), and OH reactivity (Muller et al., 2018).

Figure 2 illustrates the measurement principle of the PolyU-CIMS used in this campaign. Briefly, the ambient OH radicals are converted to H₂SO₄ in the sample inlet system by reacting with SO₂ (R21 in the reaction Table S1). These are then transformed to HSO₄⁻ ion clusters in the ionization chamber by the reactions with a reagent gas in

sheath flow (HNO_3 , R24 to 27), and ultimately dissociated (R29) for detection by the mass spectrometer system at m/z 97 ($S_{97\text{SO}_2}$ in Figure 2). To mitigate interference and noise, scavenger gases (C_3F_6 in this study) were introduced to scavenge the ambient OH, creating a background signal (R23, $S_{97\text{ScaSO}_2}$ in Figure 2). See Text S3 in the Supplementary Information for details about scavenging efficiency. The ambient OH radicals signal (S_{OH}) is then determined by subtracting $S_{97\text{ScaSO}_2}$ from $S_{97\text{SO}_2}$. The OH concentration is calculated using the following equation:

$$[\text{OH}] = \frac{1}{C_{\text{OH}}} \times \frac{S_{\text{OH}}}{S_{62}} \quad (\text{E1})$$

Where C_{OH} represents the calibration factors of OH, and S_{62} is the signal corresponding to the reagent ion (NO_3^-). The detailed calibration procedure for OH is outlined in previous studies (Kürten et al., 2012; Zou et al., 2023) and also in Text S1. Ambient and injected NO can interfere with OH measurements through reaction of $\text{NO} + \text{HO}_2$. The interference by ambient NO is estimated using a model (within a range of $10^4 - 10^5 \text{ cm}^{-3}$) and was subtracted from the ambient OH measurements (see Text S4.2). The interference from the injected NO after HO_2 measurement is discussed in Text S4.2 and is mitigated through the duty cycle configuration described in Text S5.

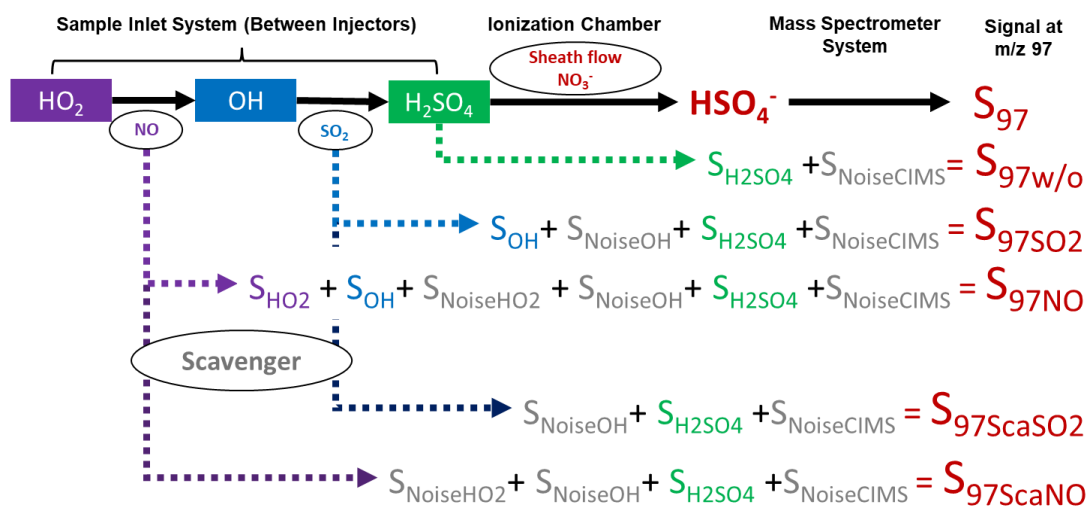


Figure 2 Flow chart depicts the relationship between measurement species and signal intensity at m/z 97 (S_{97}) with various gas injections. The color-filled grids label the ambient species, while oval shapes label the species injected into the sample flow. Signal intensities with different gas additions to the sample flow are represented by $S_{97\text{w/o}}$, $S_{97\text{SO}_2}$, $S_{97\text{NO}}$, $S_{97\text{ScaSO}_2}$, and $S_{97\text{ScaNO}}$. The signals correspond to ambient OH, HO_2 , H_2SO_4 and noise from OH measurement, HO_2 measurement and the CIMS denoted as S_{OH} , S_{HO_2} , $S_{\text{H}_2\text{SO}_4}$, S_{NoiseOH} , S_{NoiseHO_2} , and $S_{\text{NoiseCIMS}}$, respectively.

To measure ambient HO₂, NO is injected into the sample flow, converting HO₂ to OH (R11). This converted OH then follows the same reaction pathway (R21, R24 through R27, and R29) and is measured at m/z 97 (S_{97NO} in Figure 2). Similar to the OH measurement, the background signal for HO₂ (S_{97ScaNO} in Figure 2) is determined by introducing the scavenger gas. The corresponding signal for ambient HO₂ (S_{HO2}, as shown in Figure 2) is determined by subtracting S_{97ScaNO} and S_{OH} from S_{97NO}. The HO₂ concentration is calculated using an equation similar to E1, by replacing S_{OH}, and C_{OH} to S_{HO2} and C_{HO2}, respectively (E2).

$$[HO_2] = \frac{1}{C_{HO2}} \times \frac{S_{HO2}}{S_{62}} \quad (E2)$$

The procedure for determining the HO₂ calibration factor, C_{HO2}, is akin to that for C_{OH} (Text S1). The calibration tube generates equal amounts of radicals (R30 in SI, [OH]/[HO₂] = 1), allowing for simultaneous calibration of HO₂ and OH with and without NO addition to the sample flow.

In addition to HO₂, the added NO can also react with RO₂ and produce HO₂, which is a potential interference leading to an overestimation of ambient HO₂ levels (Edwards et al., 2003; Hanke et al., 2002; Fuchs et al., 2011; Whalley et al., 2013; Fuchs et al., 2014). For our CIMS configuration, the model estimated daytime interference from RO₂ ranged from 44% to 69% of the HO₂* during the field study (Text S4.3 and Figure S9). Considering the uncertainties of RO₂ mechanisms in the MCM model, we opted not to use model results to correct RO₂ interference and denote our HO₂ measurement hereafter as HO₂* which is the maximum value of the ambient HO₂ concentrations.

Compared to the configuration of PolyU-CIMS in the previous campaign (Zou et al., 2023), the instrument has been upgraded for simultaneous HO₂* measurements. Refer to Figure S2 and Text S2 for modification to HO₂* measurement and to Text S5 for measurement duty cycle. Apart from these modifications, the settings and configurations of the PolyU-CIMS remained the same as those in the previous campaign (see Table S3). With the updated configuration, the PolyU-CIMS achieved the simultaneous measurement of OH, HO₂*, and H₂SO₄.

The calibration factors, detection limits and uncertainties were $1.09 \times 10^{-8} \text{ cm}^{-3}$, $3 \times 10^5 \text{ cm}^{-3}$, and 44% for OH; $1.07 \times 10^{-8} \text{ cm}^{-3}$, $2 \times 10^6 \text{ cm}^{-3}$, and 222% for HO_2^* , respectively (Table S3). The large uncertainty in HO_2^* reflects the possible contribution of RO_2 interference, as discussed above.

2.3 Box Model

HO_x concentrations in this study were simulated using the Framework for 0-D Atmospheric Modelling (F0AM, Wolfe et al., 2016) with the Master Chemical Mechanism (MCM) v3.3.1 (<http://mcm.leeds.ac.uk/MCM>), which encompasses over 6,700 species and 17,000 reactions. MCM v3.3.1 features a near-explicit chemical mechanism that includes isoprene degradation and OH regeneration mechanisms. This mechanism has previously been employed to investigate HO_x chemistry and conducting budget analyses (Slater et al., 2020; Tan et al., 2018; Zou et al., 2023). The gas-phase chlorine chemistry described by Xu et al. (2015) and Wang et al. (2019) was included in the model (Chen et al., 2022).

In the baseline scenario, the observation data were aggregated into one-hour intervals to provide input for the model, initially constraining it without incorporating observed OH and HO_2^* data. For the assessment of ozone formation rates, the model was adjusted to include constraints based on the actual measured concentrations of OH and HO_2^* . Observed VOCs were categorized into anthropogenic origin (AVOCs), including species from petroleum gas and industrial solvent evaporation (alkenes, alkenes, benzene, and TEXs - toluene, ethylbenzene, and xylenes), and OVOCs comprising aldehydes, ketones, and acids. The sole BVOC measured in this study was isoprene. Physical processes like deposition and entrainment in the model were represented by a first-order physical loss with a 24-hour lifetime for all species (Chen et al., 2022; Wolfe et al., 2016; Zou et al., 2023). The model also included the heterogeneous uptake of HO_2 by aerosols, represented as a pseudo-first order loss (Jacob, 2000):

$$\frac{d[\text{HO}_2]}{dt} = -k_{\text{HO}_2}[\text{HO}_2] \quad (\text{E3})$$

$$k_{HO_2} = \frac{V_{HO_2} \times S_a \times \gamma_{HO_2}}{4} \quad (E4)$$

$$v_{HO_2} = \sqrt{\frac{8RT}{\pi \times M_{HO_2}}} \quad (E5)$$

Here, k_{HO_2} represents the first-order loss rate coefficient of HO_2 by aerosol uptake, determined by the effective HO_2 uptake coefficient γ_{HO_2} (0.1, Guo et al., 2019), the mean molecular velocity of HO_2 (v_{HO_2}), the aerosol surface area concentration (S_a) measured by the Scanning Mobility Particle Sizing (SMPS); and the molecular mass of HO_2 ($M_{HO_2} = 17$ g/mol). As aerosol and aqueous phase chemistry were not included in the model, it was assumed that the heterogeneous HO_2 loss would not lead to further reactions (Guo et al., 2019). For each day, a three-day spin-up was performed with constant inputs to establish stable model chemistry and reduce the uncertainty of unconstrained species. Refer to Text S4 for details on model setup for interferences assessment.

3. Results and Discussion

3.1 Results from Observations

3.1.1 Overview

Figure 3 illustrates a time series showing observed concentrations of radical and trace gases, along with meteorological parameters, from 12 November to 19 December 2022. In November, the conditions were characterised by warm temperatures ranging from 29°C to 19°C and high relative humidity averaging 86%. In contrast, December witnessed a significant decrease in temperature (ranging from 20°C to 9°C) and a reduction in relative humidity (averaging 72%). Wind speeds during the campaign were generally low, averaging 0.9 ± 0.6 m/s and typically remaining below 3.0 m/s, with higher speeds occurring towards the end of December. In November, daytime winds predominantly blew from the south, while nighttime winds came from the north. In December, northerly winds predominated both day and night. Detailed hourly wind speed and direction data are illustrated in Figure 3, and wind roses are shown in Figure S3. On days with low wind speeds (less than 0.5 m/s), NO_x emissions from the G105 national highway significantly influenced chemical measurements at the monitoring

1 site, causing morning NO levels to peak at several parts per billion (ppb). Isoprene
2 concentrations peaked in the afternoons, ranging from 0.2 to 1.7 ppb in November and
3 dropping to less than 0.1 ppb in December. Other trace gases and particulate matter
4 levels were higher in November than in December.

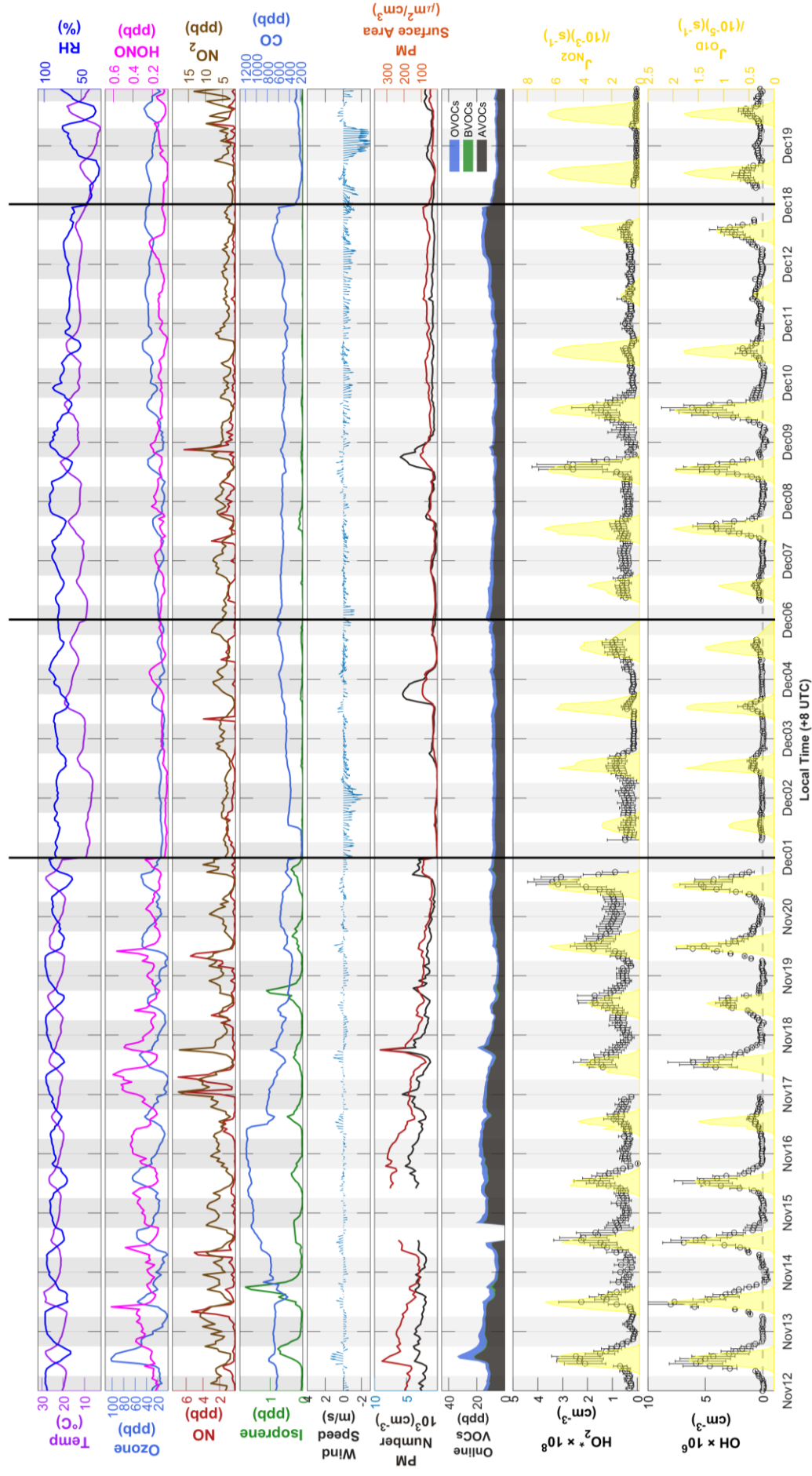


Figure 3 Time series of HO₂* and OH radicals from 12 November to 19 December, showing measured weather conditions (temperature, RH, wind speed, and wind direction), primary sources of HO_x radicals (ozone, HONO), important sinks of the radicals (CO, isoprene, and VOCs), and photolysis frequencies of NO₂ (J_{NO2}) and ozone (J_{O1D}). Non-continuous days during the campaign are delineated by a black line. The PRD, CEC, and CNC periods for further analysis were labelled in red, orange, and blue, respectively. The x-axis is in local time (+8 UTC).

Throughout the campaign, the daytime concentrations of OH and HO₂* consistently exceeded detection limits and showed distinct diurnal patterns. The OH concentrations typically peaked around midday, while the HO₂* levels reached their maximum approximately one to two hours later (Figure S4). The daily maximum concentration of OH varied significantly, ranging from $8.00 \times 10^6 \text{ cm}^{-3}$ to nearly the detection limit of $2.54 \times 10^5 \text{ cm}^{-3}$, with an average of $3.50 \pm 2.47 \times 10^6 \text{ cm}^{-3}$ (Table 1). Similarly, the daily maximum concentration of HO₂* varied from $3.42 \times 10^8 \text{ cm}^{-3}$ to $2.17 \times 10^7 \text{ cm}^{-3}$, averaging $1.34 \pm 0.93 \times 10^8 \text{ cm}^{-3}$ (Table 1). At nighttime, while the HO₂* levels generally remained above the detection threshold, the OH concentrations frequently approached the threshold. The average nighttime concentrations were $3.92 \times 10^7 \text{ cm}^{-3}$ for HO₂* and $1.64 \times 10^5 \text{ cm}^{-3}$ for OH. We compared the observed OH and HO₂* concentrations with those reported in previous studies conducted in urban, suburban, rural forest, and coastal sites. As illustrated in Figure S5, the OH concentrations were generally lower than those found in urban settings but similar to levels observed in suburban, rural, and forest environments. This suggests a moderate level of anthropogenic activity typical of mixed rural settings. In contrast, the HO₂* concentrations during these periods were significantly lower than earlier observations in rural and forest environments, likely owing to reduced photochemical activity during our measurement period.

Table 1 Average concentrations and standard deviation of measured species throughout the entire campaign (Total) and the selected 3 days cases from each cluster (PRD, CEC and CNC).

Species (Unit)	Total	PRD	CEC	CNC
AveMax OH _{Obs} 10 ⁶ (cm ⁻³)	3.5±2.5	6.9±1.1	4.9±1.5	5.3±0.9
OH _{Obs} 10 ⁶ (cm ⁻³)	0.9±1.5	1.6±2.2	1.4±1.6	1.2±1.8
OH _{DL} 10 ⁶ (cm ⁻³)	0.5±0.3	0.4±0.3	0.4±0.2	0.9±0.6
AveMax HO ₂ _{Obs} 10 ⁸ (cm ⁻³)	1.34±0.93	2.32±1.25	2.36±0.92	1.82±1.02
HO ₂ * _{Obs} 10 ⁸ (cm ⁻³)	0.59±0.51	0.76±0.63	1.10±0.68	0.67±0.55
HO ₂ * _{DL} 10 ⁸ (cm ⁻³)	0.19±0.11	0.17±0.10	0.25±0.08	0.26±0.15
Pressure (hpa)	995±4	992±1	992±1	995±2
Temp (°C)	16±6.1	23±3.0	23±2.6	14±2.8
RH (%)	78±15	87±11	86±10	81±9.4
Wind Speed (m/s)	0.91±0.65	0.53±0.32	0.57±0.34	0.87±0.5
j _{OH} 10 ⁻⁶ (s ⁻¹)	3.2±5.4	3.5±6	3.6±5.9	4.0±6.6
j _{NO₂} 10 ⁻³ (s ⁻¹)	1.3±1.9	1.3±2.1	1.4±2	1.6±2.3
HONO	0.169±0.104	0.249±0.084	0.201±0.070	0.133±0.033
SO ₂	0.5±0.8	0.5±0.6	0.4±0.5	0.4±0.5
NO ₂	4.89±2.37	6.25±2.47	4.84±2.23	4.52±1.97
NO	0.57±0.86	0.73±1.09	0.69±1.00	0.73±0.85
CO	557.36±225.92	739.41±153.84	464.73±74.34	513.36±22.02
Ozone	25±14	32±23	24±13	19±9.4
Particle Surface Area (um ² /cm ³)	86±72	186±51	84±28	48±19
Isoprene	0.082±0.174	0.257±0.337	0.155±0.200	0.029±0.030
*OVOCs	2.218±1.056	3.163±2.324	1.755±0.379	1.730±0.330
*AVOCs	8.346±3.223	9.662±5.031	6.886±1.755	6.801±0.864
*TEXs	0.356±0.316	0.801±0.616	0.266±0.090	0.237±0.085

Notes: Concentrations are expressed in parts per billion (ppb) unless otherwise specified. Total VOCs concentrations are categorized by origin (AVOCs and OVOCs). For the average concentration of each measured VOC, refer to Table S5.

Figure 4 illustrates the results of the 24-hour backward trajectory analysis, revealing three distinct but sequentially occurring phases. In the initial phase (Figure 4a), air masses originated from the urban and industrial zones of the Pearl River Delta (PRD). This phase was characterised by intense photochemical activity, with ambient temperatures exceeding 20°C and relative humidity levels surpassing 70%. During this period, notably high concentrations of VOCs, ozone, and radicals were observed, with the average daily maximum concentrations of OH and HO₂* radicals reaching $6.50 \pm 1.19 \times 10^6 \text{ cm}^{-3}$ and $2.20 \pm 0.27 \times 10^8 \text{ cm}^{-3}$, respectively. The subsequent phase was characterised by air masses originating from Central East China (CEC, Figure 4b). This phase showed reduced photochemical reactivity and lower concentrations of the measured trace gases. The average daily maximum concentrations of OH and HO₂* during this phase were $4.35 \pm 2.19 \times 10^6 \text{ cm}^{-3}$ and $1.96 \pm 0.90 \times 10^8 \text{ cm}^{-3}$, respectively. The final phase was influenced by air masses from Central North China (CNC, Figure

4c), which exhibited the lowest concentrations of trace gases and the least pronounced average daily maximum concentrations in OH and HO₂* concentrations, measured at $2.23 \pm 1.95 \times 10^6 \text{ cm}^{-3}$ and $7.63 \pm 7.66 \times 10^7 \text{ cm}^{-3}$, respectively. This phase coincided with an increase in cloudy days and a decrease in temperatures, indicating reduced photochemical conditions.

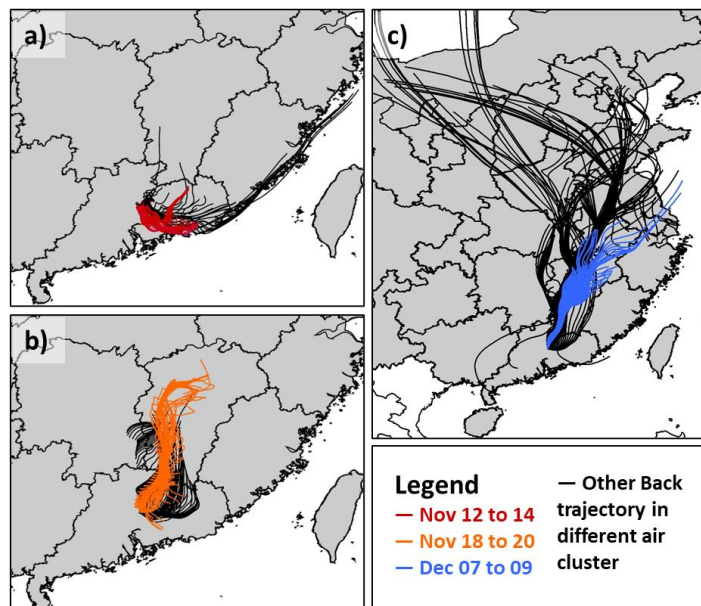


Figure 4 24-hour back trajectories for (a) Pearl River Delta (5 days), (b) Central East China (4 days), and (c) Central North China (14 days) cases. Three days selected from each cluster for model simulation are distinguished by different colours.

3.1.2 Selection of Cases

For each phase, a representative three-day period was selected for detailed analysis based on the availability of comprehensive data and sunny conditions (colored trajectories in Figure 4). In the subsequent analysis, 'PRD,' 'CEC,' and 'CNC' refer to the selected periods corresponding to the air masses originating from these regions. The average daily maximum concentrations of OH and HO₂* radicals for these periods are presented in Table 1. The average daily max OH concentrations were $6.89 \pm 1.10 \times 10^6 \text{ cm}^{-3}$ in PRD, $4.90 \pm 1.47 \times 10^6 \text{ cm}^{-3}$ in CEC, and $5.27 \pm 0.89 \times 10^6 \text{ cm}^{-3}$ in CNC, with a pronounced decrease from PRD to CEC (of $1.99 \times 10^6 \text{ cm}^{-3}$). The average daily max HO₂* concentrations were $2.32 \pm 1.25 \times 10^8 \text{ cm}^{-3}$ in PRD, $2.36 \pm 0.92 \times 10^8 \text{ cm}^{-3}$ in CEC, and $1.82 \pm 1.02 \times 10^8 \text{ cm}^{-3}$ in CNC, with a slight increase of $0.04 \times 10^8 \text{ cm}^{-3}$ from

PRD to CEC and a more substantial decrease of $0.54 \times 10^8 \text{ cm}^{-3}$ from CEC to CNC. These trends suggest a declining atmospheric oxidation capacity from PRD to CNC.

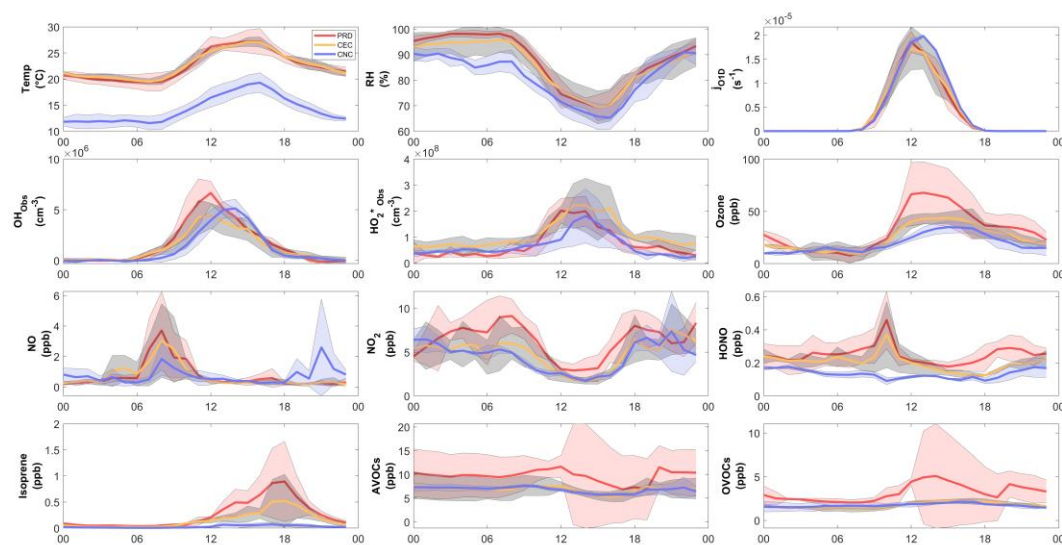


Figure 5 Average diurnal variations of (a) Temperature (b) Relative Humidity (c) J_{O1D} (d) OH (e) HO_2^* (f) Ozone (g) NO (h) NO_2 (i) HONO (j) Isoprene (k) AVOCs (l) OVOCs. The solid-colored lines represent selected cases: orange for PRD, green for CEC, and blue for CNC. The light band represents the standard deviations of the mean. The increase in the standard deviations of VOCs and OVOCs during the PRD case is a result of absence of data on the afternoon of November 14th and large variations in on November 12th and 13th.

The precursor concentrations and meteorological parameters also varied across cases in terms of statistics (Tables 1 and S4) and diurnal variations (Figure 5). In the PRD case, the average concentrations are characteristic of a rural environment, with AVOCs at 9.70 ± 5.00 ppb, OVOCs at 3.20 ± 2.30 ppb, isoprene at 0.26 ± 0.34 ppb, NO_2 at 6.3 ± 2.5 ppb, and NO at 0.73 ± 1.09 ppb. The NO concentration was affected by traffic sources, as there were no other fresh emission source nearby, and the diurnal variation of NO showed a morning peak in all three cases (Figure 5). In the CEC case, a general reduction in anthropogenic influence is evident. AVOCs, OVOCs isoprene and NO_2 drop significantly to 6.90 ± 1.80 ppb, 1.70 ± 0.38 ppb, 0.16 ± 0.20 ppb, and 4.84 ± 2.23 ppb respectively. Meanwhile, NO levels remained close to PRD levels at 0.69 ± 1.00 ppb. In the CNC case, the air mass was more aged with reduced biogenic emissions, reflected in further decreases in isoprene and NO_2 to 0.03 ± 0.04 ppb and 4.52 ± 1.97 ppb, respectively, due to colder weather conditions. The temperature

decreased significantly from PRD to CNC, whereas the average peak photolysis frequency was comparable between PRD and CNC, as shown in Table 1.

3.2 Chemical budgets of OH and HO₂

To investigate the OH and HO₂ chemical budgets during the three distinct periods, we employed a box model constrained by observed concentrations of NO_x, VOCs, and relevant meteorological parameters in the selected cases (base scenario in which OH and HO₂ concentrations were not constrained by the measurements). The resulting OH and HO₂ budgets, displaying typical bell-shaped patterns, are illustrated in Figure 6. During midday (10:00–15:00), the recycling of RO species becomes the dominant pathway for HO₂ production, with rates of 3.22 ppb h⁻¹ for PRD, 2.09 ppb h⁻¹ for CEC, and 1.08 ppb h⁻¹ for CNC. Additionally, HCHO photolysis contributed 0.75 ppb h⁻¹, 0.46 ppb h⁻¹, and 0.26 ppb h⁻¹ for PRD, CEC, and CNC, respectively. The sinks of HO₂ varied among the cases with minor contribution from the uptake process, driven by radical termination mechanisms. The rate of radical self-reactions decreased from PRD to CNC. In contrast, NO_x-radical reactions between CEC and CNC were comparable, with respective rates of 0.39 ppb h⁻¹ and 0.33 ppb h⁻¹, indicating a shift in radical termination mechanisms.

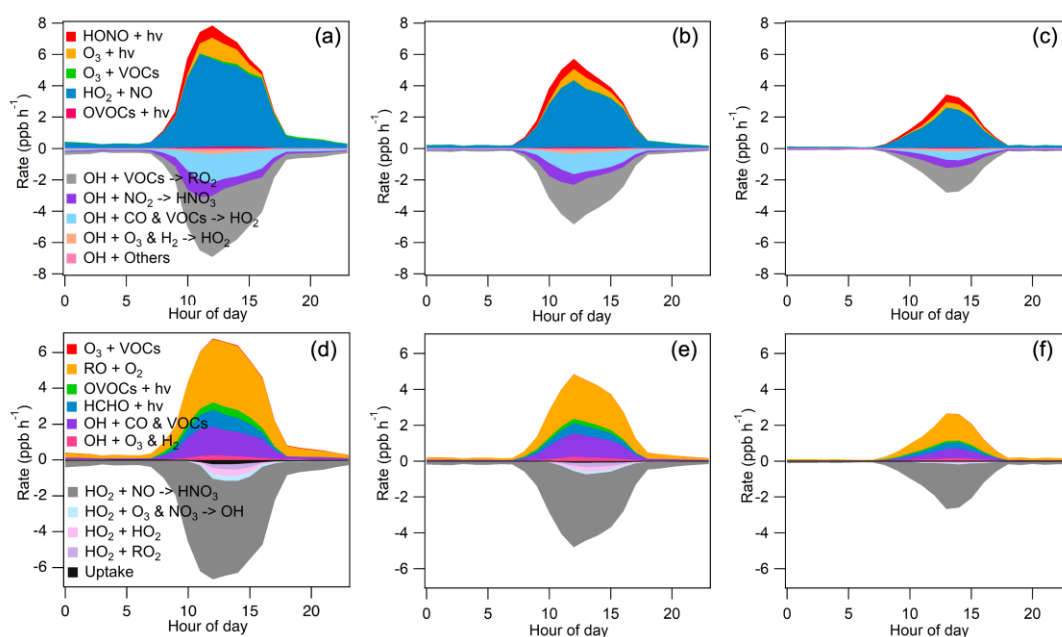


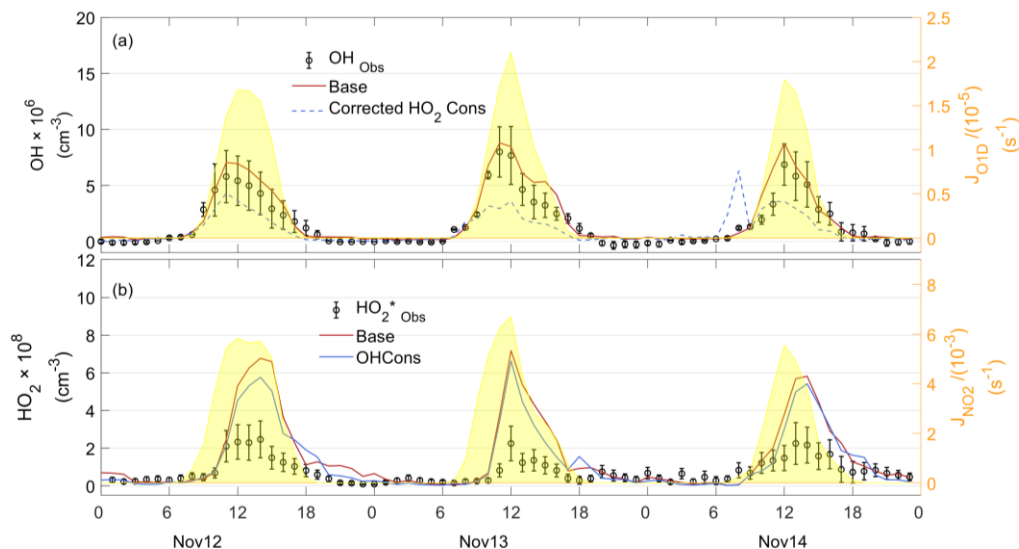
Figure 6 Chemical budgets of OH and HO₂ for PRD (a, d), CEC (b, e), and CNC (c, f) simulated using a chemical box model.

OH formation was predominantly driven by the $\text{HO}_2 + \text{NO}$ reaction, contributing 5.18 ppb h^{-1} , 3.51 ppb h^{-1} , and 1.81 ppb h^{-1} (average for 10:00 – 15:00, referred to hereafter in this section) for PRD, CEC, and CNC, respectively. Additionally, contributions from ozone photolysis and HONO increased from PRD to CEC and then to CNC, with rates of 21.4%, 22.7%, and 24.6%, respectively. The primary sinks for OH included reactions with VOCs to produce RO_2 , with rates of 3.31 ppb h^{-1} , 2.02 ppb h^{-1} , and 1.13 ppb h^{-1} , and reactions with CO and other VOCs to generate HO_2 , contributing 1.55 ppb h^{-1} , 1.06 ppb h^{-1} , and 0.38 ppb h^{-1} for PRD, CEC, and CNC, respectively. These findings highlight the critical role of OH + VOC reactions in the chemical budget of OH.

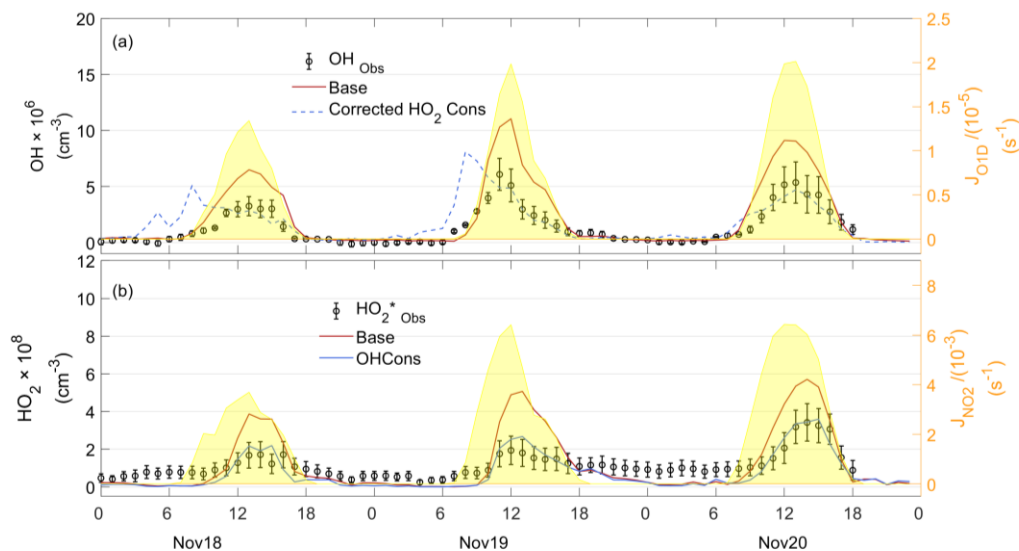
3.3 Comparison of model with observation results

Modeled OH and HO_2 concentrations were evaluated by comparing them against observations. The observed HO_2^* serves as an upper limit for ambient HO_2 due to the interference from RO_2 . According to model simulations (Text S4.3), RO_2 interference was estimated to account for 56%, 54%, and 59% of the observed HO_2^* signal for the PRD, CEC and CNC case, respectively. In the PRD case (Figure 7), which represents the most polluted and warmest environment among the three cases, the model slightly overestimated OH concentrations. However, the modeled HO_2 concentration was substantially higher than the observed HO_2^* , indicating an overprediction of HO_2 . Similar overestimations have been reported at a rural site (Kanaya et al., 2012). For the CEC case (Figure 8), the modeled OH and HO_2 concentrations were moderately higher than the observed values during the daytime, consistent with findings from a rural forest site (Bottorff et al., 2023). In the CNC case (Figure 9), the model generally reproduced the observed OH trend, with HO_2 comparable to the observed HO_2^* . However, on December 7, it exhibited daytime overestimation of HO_x , similar to the PRD case. At night, both CNC and CEC showed lower modeled HO_2 concentrations compared to observed HO_2^* , which can be explained by the expected contribution of RO_2 interference to HO_2^* in the observations. To further investigate the possible reasons for the model-observation discrepancies, sensitivity tests were conducted. The modeled

1 RO₂ interference ratio was used to correct HO₂* values, roughly estimating ambient
 2 HO₂ as input for the tests.



3 **Figure 7** observed and simulated OH, observed HO₂*, and simulated HO₂ time series for the PRD
 4 case. The “Obs” subscript denotes the observation data. “Base” denotes the result of Baseline
 5 scenario as described in Box Model section. “Cons” denotes the results with additional constrained
 6 species compared to Base.
 7



8 **Figure 8** observed and simulated OH, observed HO₂*, and simulated HO₂ time series for the CEC
 9 case. The “Obs” subscript denotes the observation data. “Base” denotes the result of Baseline
 10 scenario as described in Box Model section. “Cons” denotes the results with additional constrained
 11 species compared to Base.
 12

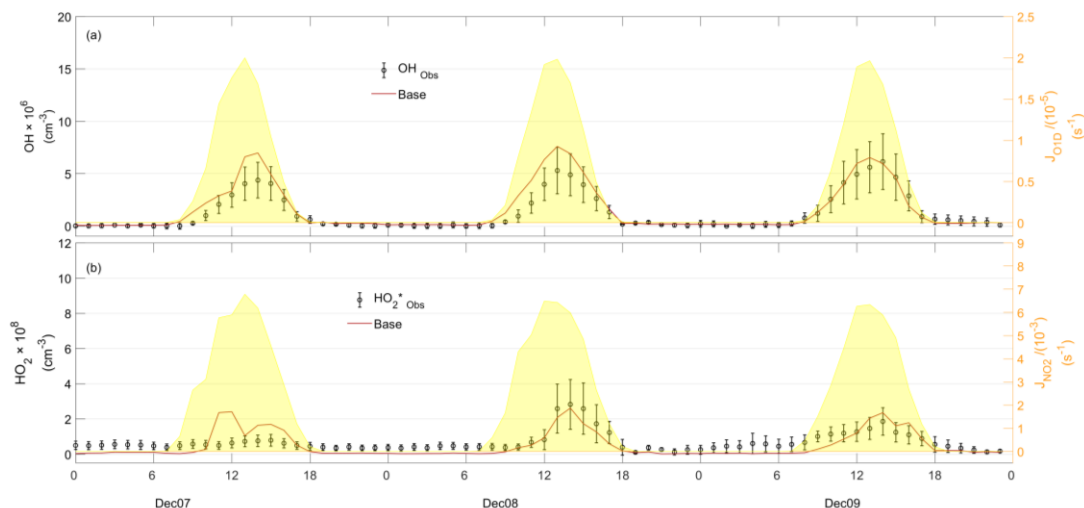


Figure 9 observed and simulated time series of OH and HO₂* for the CNC case. “Base” denotes the result of Baseline scenario as described in Box Model section.

3.3.1 Substantial overestimation of HO₂ in PRD case

To explain the HO₂ overprediction by the base model, we constrained OH or corrected HO₂* and compared these to the base case (without constraining OH and HO₂). Result shows that constraining corrected HO₂* (blue line in Figure 7a) causes the model to underestimate OH, while constraining OH still leads substantially higher modeled HO₂ concentration (blue line in Figure 7b) than the observed HO₂*. This result suggests that to align the modeled OH and HO₂ with observations, it may be necessary to introduce a strong, unknown process for HO₂ that efficiently recycles OH with a high yield (Kanaya et al., 2012).

3.3.2 Moderate overestimation of both OH and HO₂ radicals in CEC case

Unlike the PRD case, constraining either OH or corrected HO₂* in the CEC case generally reduces the daytime overestimation of both HO₂ and OH. These results indicate an additional sink for both OH and HO₂, as suggested by Bottorff et al. (2023). However, the OH concentration is overestimated in the morning when the corrected HO₂* was constrained, suggesting that some OH sinks may be missing in the model during this period or the corrected HO₂* values that were used to constrain the model are still higher than the true HO₂ values. To further investigate the underlying causes, we examined the correlations between various pollutants. The significant negative correlation between CO and NO ($R^2=0.49$, $p=0.01$, Figure S6b) suggests that morning

conditions in the CEC case may have been influenced by emission from fresh complete combustion during the CEC case, while correlations in the PRD and CNC cases are not significant (Figures S6a and c). This indicates that the missing OH reactivity in the CEC case during the morning hours is possibly related to fresh vehicle emissions.

4. Implication for model overestimation of HO_x

OH and HO₂ are key species that determine the atmosphere's oxidative processes. Inaccurate modelling of their sinks can lead to significant overestimations of oxidation capacity, which may skew assessments of the impact of HO_x on air pollution and climate change. This problem is particularly pronounced in the case of ozone, a widespread photochemical pollutant. To demonstrate this issue, we compared results from two modelling scenarios: the first scenario was base case (as described in section 3.2), while the second scenario included constraints from all observational parameters, including measurements of OH and HO₂^{*}. Results for the scenario constrained by OH and corrected HO₂^{*} measurements are also showed in Figures 10 and 11.

As illustrated in Figure 10, not constraining free-radical measurement data in the chemical model (the orange lines) led to overestimates of ozone's photochemical production rates. Compared to scenarios constrained by OH and HO₂^{*}, in the PRD case, simulated midday O_x (O₃ + NO₂) formation rates in the base case were overestimated by 33% on average and 32% at peak O_x rates. In the CEC case, the overestimation was 79% on average and 89% at peak O_x rates, while in the CNC case, the smallest overestimation was 17% on average and 25% at peak. Since the ambient HO₂ concentration is lower than the constrained HO₂^{*} concentration, the impact of the overestimated HO_x on ozone production rates might be even larger in such environments (the green lines in Figure 10).

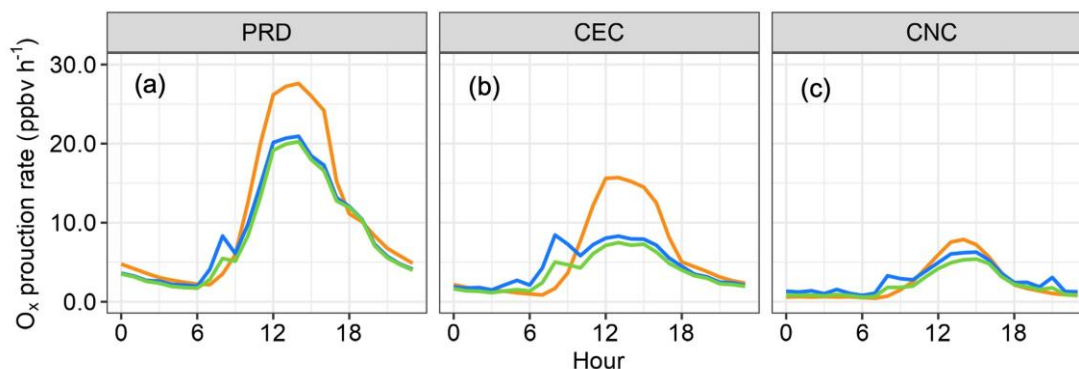


Figure 10 O_X (O_3+NO_2) photochemical production rates in three comparative cases: (a) PRD, (b) CEC, and (c) CNC. The orange, green, and blue lines represent rates modelled by excluding OH and HO_2^* , including OH with corrected HO_2^* , and including OH with uncorrected HO_2^* , respectively.

The overestimation of HO_X also significantly affected the simulated concentration of nitric acid (HNO_3), which is crucial for new particle formation and growth (Wang et al., 2020). Figure 11 illustrates that the chemical model moderately overestimated nitric acid production rates without the constraints of free-radical measurements (the orange lines). Compared to the scenarios constrained by OH and HO_2^* , the midday production rates of nitric acid were overestimated by 25%, 88%, and 31% in the PRD, CEC, and CNC cases, respectively. Such overestimations can considerably impact assessments of new particle formation and growth processes and their impact on air pollution and climate change. On the other hand, the impact on HNO_3 production is dominated by OH radical, therefore, measurement interference of HO_2 is negligible.

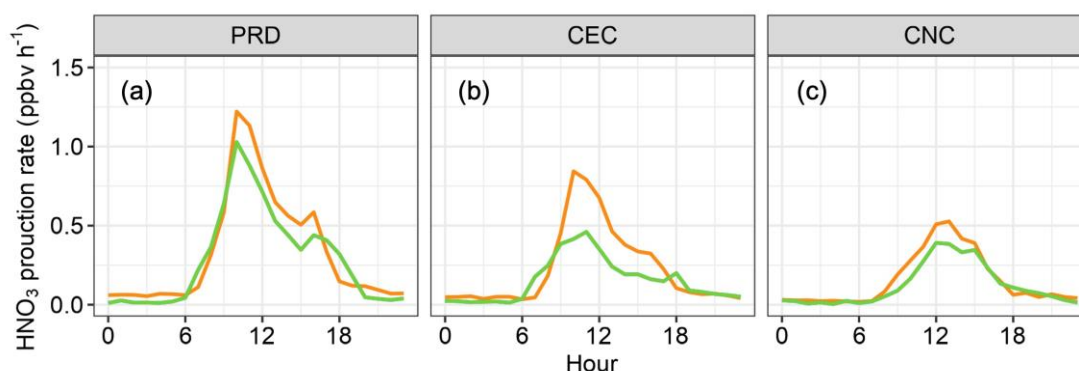


Figure 11 Modelled HNO_3 production rates in three comparative cases: (a) PRD, (b) CEC, and (c) CNC. The orange, green, and blue lines represent rates modelled by excluding OH and HO_2^* , including OH with corrected HO_2^* , and including OH with uncorrected HO_2^* , respectively. [The

blue lines are covered by the green lines as the daytime HNO_3 production rate are determined by the constrained OH].

5. Conclusion

HO_2^* and OH concentrations were measured using a chemical ionization mass spectrometer at a subtropical rural site in southern China from 12 November to 19 December 2022. The measurements indicated generally lower concentrations of OH and HO_2^* than those observed in previous studies at various sites. The model estimated that interferences from RO_2 contributed to 44%-69% of the HO_2^* throughout the campaign. Backward trajectory analysis revealed three distinct phases characterised by sequentially decreasing pollution levels and temperatures. During the cold, clean period, model simulations closely matched the observed OH and HO_2^* concentrations. However, during the warm, polluted period, the models overestimated HO_2 or both radicals. Model sensitivity analysis indicates that adding an OH cycling reaction from HO_2 or additional sinks of OH and HO_2 would largely reduce the model-observation discrepancy in different cases of this study. However, the exact chemical reactions remain to be identified. Our results are in line with previous studies indicating substantial gaps in our understanding of the sources and sinks of OH and HO_2 in certain environments. Our study provides additional evidence for the current incomplete understanding of the HO_x sources and sinks and calls for more research to resolve the model–observation mismatch found in this work and in previous studies.

The over-prediction of HO_x resulted in significant overestimation of the production rates of other secondary pollutants such as ozone and nitric acid at the site. It is critical to evaluate the capability of OH and HO_2 simulations in major chemical transport models and earth system models, as inaccurate simulations of OH and HO_2 may misguide the development of air pollution and global warming control strategies.

Data availability. All of the data used to produce this paper can be obtained by contacting Tao Wang (tao.wang@polyu.edu.hk).

Supplement. The online supplement for this article is available at:

Author contributions. TW conceived the HO_x research. TW, XW and YZ planned and organized the overall field campaign at Conghua. ZZ conducted the HO_x measurements using CIMS, with contributions from TW and WS, QC, and SH. XF, ZR, XL, AG, QW, CP, and XT performed the JNO₂ VOCs and OVOCs measurements. ZZ performed the chemical box modelling with contributions from TC and QC. TC, ZZ, and TW analysed the data and interpreted the result (ZZ analysed the time series and diurnal variations of observation data; TC interpreted the results of box model, investigated the missing sources; TW supervised and guided these processes). TC, ZZ, and TW wrote the paper. All of the authors reviewed and commented on the paper.

Competing interests. One author (Tao Wang) is a member of the editorial board of Atmospheric Chemistry and Physics. The authors have no other competing interests to declare.

Acknowledgments

We thank David Tanner, Dr. Wei Pu, Dr. Weihao Wang, and Dr. Zhe Wang for developing the PolyU-CIMS. We are also grateful to the Guangzhou Institute of Geochemistry, Chinese Academy of Sciences, for providing access to its station and data on trace gases.

Financial support.

This research was financially supported by the Hong Kong Research Grants Council (T24-504/17-N and 15223221 to Tao Wang), the National Science Foundation of China (42293322 to Tao Wang), and The Hong Kong Polytechnic University Postdoc Matching Fund Scheme (P0043403 to Tianshu Chen).

Reference

Berresheim, H., Elste, T., Tremmel, H. G., Allen, A. G., Hansson, H.-C., Rosman, K., Dal Maso, M., Mäkelä, J. M., Kulmala, M., and O'Dowd, C. D.: Gas-aerosol relationships of H₂SO₄, MSA, and OH: Observations in the coastal marine boundary layer at Mace Head, Ireland, Journal of Geophysical Research: Atmospheres, 107, PAR 5-1-PAR 5-12, <https://doi.org/10.1029/2000JD000229>, 2002.

Bottorff, B., Lew, M. M., Woo, Y., Rickly, P., Rollings, M. D., Deming, B., Anderson, D. C., Wood,

1 E., Alwe, H. D., Millet, D. B., Weinheimer, A., Tyndall, G., Ortega, J., Dusanter, S., Leonardis, T.,
2 Flynn, J., Erickson, M., Alvarez, S., Rivera-Rios, J. C., Shutter, J. D., Keutsch, F., Helmig, D., Wang,
3 W., Allen, H. M., Slade, J. H., Shepson, P. B., Bertman, S., and Stevens, P. S.: OH, HO₂, and RO₂
4 radical chemistry in a rural forest environment: measurements, model comparisons, and
5 evidence of a missing radical sink, *Atmospheric Chemistry and Physics*, 23, 10287–10311,
6 <https://doi.org/10.5194/acp-23-10287-2023>, 2023.

7 Carslaw, N., Creasey, D. J., Heard, D. E., Lewis, A. C., McQuaid, J. B., Pilling, M. J., Monks, P. S.,
8 Bandy, B. J., and Penkett, S. A.: Modeling OH, HO₂, and RO₂ radicals in the marine boundary
9 layer: 1. Model construction and comparison with field measurements, *J. Geophys. Res.*, 104,
10 30241–30255, <https://doi.org/10.1029/1999JD900783>, 1999.

11 Chen, Q., Xia, M., Peng, X., Yu, C., Sun, P., Li, Y., Liu, Y., Xu, Z., Xu, Z., Wu, R., Nie, W., Ding, A.,
12 Zhao, Y., and Wang, T.: Large Daytime Molecular Chlorine Missing Source at a Suburban Site
13 in East China, *JGR Atmospheres*, 127, <https://doi.org/10.1029/2021JD035796>, 2022.

14 Edwards, G. D., Cantrell, C. A., Stephens, S., Hill, B., Goyea, O., Shetter, R. E., Mauldin, R. L.,
15 Kosciuch, E., Tanner, D. J., and Eisele, F. L.: Chemical Ionization Mass Spectrometer Instrument
16 for the Measurement of Tropospheric HO₂ and RO₂, *Anal. Chem.*, 75, 5317–5327,
17 <https://doi.org/10.1021/ac034402b>, 2003.

18 Eisele, F. L. and Tanner, D. J.: Ion-assisted tropospheric OH measurements, *J. Geophys. Res.*,
19 96, 9295, <https://doi.org/10.1029/91JD00198>, 1991.

20 Eisele, F. L. and Tanner, D. J.: Measurement of the gas phase concentration of H₂SO₄ and
21 methane sulfonic acid and estimates of H₂SO₄ production and loss in the atmosphere, *Journal*
22 *of Geophysical Research: Atmospheres*, 98, 9001–9010, <https://doi.org/10.1029/93JD00031>,
23 1993.

24 Feiner, P. A., Brune, W. H., Miller, D. O., Zhang, L., Cohen, R. C., Romer, P. S., Goldstein, A. H.,
25 Keutsch, F. N., Skog, K. M., Wennberg, P. O., Nguyen, T. B., Teng, A. P., DeGouw, J., Koss, A.,
26 Wild, R. J., Brown, S. S., Guenther, A., Edgerton, E., Baumann, K., and Fry, J. L.: Testing
27 Atmospheric Oxidation in an Alabama Forest, *Journal of the Atmospheric Sciences*, 73, 4699–
28 4710, <https://doi.org/10.1175/JAS-D-16-0044.1>, 2016.

29 Fuchs, H., Bohn, B., Hofzumahaus, A., Holland, F., Lu, K. D., Nehr, S., Rohrer, F., and Wahner,
30 A.: Detection of HO₂ by laser-induced fluorescence: calibration and interferences from RO₂
31 radicals, *Atmospheric Measurement Techniques*, 4, 1209–1225, [https://doi.org/10.5194/amt-](https://doi.org/10.5194/amt-4-1209-2011)
32 [4-1209-2011](https://doi.org/10.5194/amt-4-1209-2011), 2011.

33 Fuchs, H., Acir, I.-H., Bohn, B., Brauers, T., Dorn, H.-P., Häseler, R., Hofzumahaus, A., Holland,
34 F., Kaminski, M., Li, X., Lu, K., Lutz, A., Nehr, S., Rohrer, F., Tillmann, R., Wegener, R., and Wahner,
35 A.: OH regeneration from methacrolein oxidation investigated in the atmosphere simulation
36 chamber SAPHIR, *Atmos. Chem. Phys.*, 14, 7895–7908, [https://doi.org/10.5194/acp-14-7895-](https://doi.org/10.5194/acp-14-7895-2014)
37 [2014](https://doi.org/10.5194/acp-14-7895-2014), 2014.

1 Griffith, S. M., Hansen, R. F., Dusanter, S., Stevens, P. S., Alaghmand, M., Bertman, S. B., Carroll,
2 M. A., Erickson, M., Galloway, M., Grossberg, N., Hottle, J., Hou, J., Jobson, B. T., Kammrath, A.,
3 Keutsch, F. N., Lefer, B. L., Mielke, L. H., O'Brien, A., Shepson, P. B., Thurlow, M., Wallace, W.,
4 Zhang, N., and Zhou, X. L.: OH and HO₂ radical chemistry during PROPHET 2008 and CABINEX
5 2009 – Part 1: Measurements and model comparison, *Atmospheric Chemistry and Physics*, 13,
6 5403–5423, <https://doi.org/10.5194/acp-13-5403-2013>, 2013.

7 Guo, J., Wang, Z., Tao Wang, and Zhang, X.: Theoretical evaluation of different factors
8 affecting the HO₂ uptake coefficient driven by aqueous-phase first-order loss reaction,
9 *Science of The Total Environment*, 683, 146–153,
10 <https://doi.org/10.1016/j.scitotenv.2019.05.237>, 2019.

11 Hanke, M., Uecker, J., Reiner, T., and Arnold, F.: Atmospheric peroxy radicals: ROXMAS, a new
12 mass-spectrometric methodology for speciated measurements of HO₂ and Σ RO₂ and first
13 results, *International Journal of Mass Spectrometry*, 213, 91–99,
14 [https://doi.org/10.1016/S1387-3806\(01\)00548-6](https://doi.org/10.1016/S1387-3806(01)00548-6), 2002.

15 Hansen, R. F., Griffith, S. M., Dusanter, S., Rickly, P. S., Stevens, P. S., Bertman, S. B., Carroll, M.
16 A., Erickson, M. H., Flynn, J. H., Grossberg, N., Jobson, B. T., Lefer, B. L., and Wallace, H. W.:
17 Measurements of total hydroxyl radical reactivity during CABINEX 2009 – Part 1: field
18 measurements, *Atmos. Chem. Phys.*, 14, 2923–2937, [https://doi.org/10.5194/acp-14-2923-](https://doi.org/10.5194/acp-14-2923-2014)
19 2014, 2014.

20 Heard, D. E. and Pilling, M. J.: Measurement of OH and HO₂ in the Troposphere, *Chem. Rev.*,
21 103, 5163–5198, <https://doi.org/10.1021/cr020522s>, 2003.

22 Hens, K., Novelli, A., Martinez, M., Auld, J., Axinte, R., Bohn, B., Fischer, H., Keronen, P., Kubistin,
23 D., Nölscher, A. C., Oswald, R., Paasonen, P., Petäjä, T., Regelin, E., Sander, R., Sinha, V., Sipilä,
24 M., Taraborrelli, D., Tatum Ernest, C., Williams, J., Lelieveld, J., and Harder, H.: Observation and
25 modelling of HO_x radicals in a boreal forest, *Atmospheric Chemistry and Physics*, 14, 8723–
26 8747, <https://doi.org/10.5194/acp-14-8723-2014>, 2014.

27 Hofzumahaus, A., Rohrer, F., Lu, K., Bohn, B., Brauers, T., Chang, C.-C., Fuchs, H., Holland, F.,
28 Kita, K., Kondo, Y., Li, X., Lou, S., Shao, M., Zeng, L., Wahner, A., and Zhang, Y.: Amplified Trace
29 Gas Removal in the Troposphere, *Science*, 324, 1702–1704,
30 <https://doi.org/10.1126/science.1164566>, 2009.

31 Jacob, D.: Heterogeneous chemistry and tropospheric ozone, *Atmospheric Environment*, 34,
32 2131–2159, [https://doi.org/10.1016/S1352-2310\(99\)00462-8](https://doi.org/10.1016/S1352-2310(99)00462-8), 2000.

33 Jeong, D., Seco, R., Emmons, L., Schwantes, R., Liu, Y., McKinney, K. A., Martin, S. T., Keutsch,
34 F. N., Gu, D., Guenther, A. B., Vega, O., Tota, J., Souza, R. A. F., Springston, S. R., Watson, T. B.,
35 and Kim, S.: Reconciling Observed and Predicted Tropical Rainforest OH Concentrations, *JGR*
36 *Atmospheres*, 127, <https://doi.org/10.1029/2020JD032901>, 2022.

37 Kanaya, Y., Cao, R., Kato, S., Miyakawa, Y., Kajii, Y., Tanimoto, H., Yokouchi, Y., Mochida, M.,

- 1 Kawamura, K., and Akimoto, H.: Chemistry of OH and HO₂ radicals observed at Rishiri Island,
2 Japan, in September 2003: Missing daytime sink of HO₂ and positive nighttime correlations
3 with monoterpenes, *J. Geophys. Res.*, 112, D11308, <https://doi.org/10.1029/2006JD007987>,
4 2007.
- 5 Kanaya, Y., Hofzumahaus, A., Dorn, H.-P., Brauers, T., Fuchs, H., Holland, F., Rohrer, F., Bohn,
6 B., Tillmann, R., Wegener, R., Wahner, A., Kajii, Y., Miyamoto, K., Nishida, S., Watanabe, K.,
7 Yoshino, A., Kubistin, D., Martinez, M., Rudolf, M., Harder, H., Berresheim, H., Elste, T., Plass-
8 Dülmer, C., Stange, G., Kleffmann, J., Elshorbany, Y., and Schurath, U.: Comparisons of
9 observed and modeled OH and HO₂ concentrations during the ambient measurement period
10 of the HO_xComp field campaign, *Atmospheric Chemistry and Physics*, 12, 2567–2585,
11 <https://doi.org/10.5194/acp-12-2567-2012>, 2012.
- 12 Kim, S., Wolfe, G. M., Mauldin, L., Cantrell, C., Guenther, A., Karl, T., Turnipseed, A., Greenberg,
13 J., Hall, S. R., Ullmann, K., Apel, E., Hornbrook, R., Kajii, Y., Nakashima, Y., Keutsch, F. N., DiGangi,
14 J. P., Henry, S. B., Kaser, L., Schnitzhofer, R., Graus, M., Hansel, A., Zheng, W., and Flocke, F. F.:
15 Evaluation of HO_x sources and cycling using measurement-constrained model calculations in
16 a 2-methyl-3-butene-2-ol (MBO) and monoterpene (MT) dominated ecosystem,
17 *Atmospheric Chemistry and Physics*, 13, 2031–2044, [https://doi.org/10.5194/acp-13-2031-](https://doi.org/10.5194/acp-13-2031-2013)
18 2013, 2013.
- 19 Kürten, A., Rondo, L., Ehrhart, S., and Curtius, J.: Calibration of a Chemical Ionization Mass
20 Spectrometer for the Measurement of Gaseous Sulfuric Acid, *J. Phys. Chem. A*, 116, 6375–
21 6386, <https://doi.org/10.1021/jp212123n>, 2012.
- 22 Lelieveld, J., Butler, T. M., Crowley, J. N., Dillon, T. J., Fischer, H., Ganzeveld, L., Harder, H.,
23 Lawrence, M. G., Martinez, M., Taraborrelli, D., and Williams, J.: Atmospheric oxidation capacity
24 sustained by a tropical forest, *Nature*, 452, 737–740, <https://doi.org/10.1038/nature06870>,
25 2008.
- 26 Lew, M. M., Rickly, P. S., Bottorff, B. P., Reidy, E., Sklaveniti, S., Léonardis, T., Locoge, N.,
27 Dusanter, S., Kundu, S., Wood, E., and Stevens, P. S.: OH and HO₂ radical chemistry in a
28 midlatitude forest: measurements and model comparisons, *Atmospheric Chemistry and*
29 *Physics*, 20, 9209–9230, <https://doi.org/10.5194/acp-20-9209-2020>, 2020.
- 30 Lou, S., Holland, F., Rohrer, F., Lu, K., Bohn, B., Brauers, T., Chang, C. C., Fuchs, H., Häsel, R.,
31 Kita, K., Kondo, Y., Li, X., Shao, M., Zeng, L., Wahner, A., Zhang, Y., Wang, W., and Hofzumahaus,
32 A.: Atmospheric OH reactivities in the Pearl River Delta – China in summer 2006: measurement
33 and model results, *Atmos. Chem. Phys.*, 10, 11243–11260, [https://doi.org/10.5194/acp-10-](https://doi.org/10.5194/acp-10-11243-2010)
34 11243-2010, 2010.
- 35 Ma, X., Tan, Z., Lu, K., Yang, X., Liu, Y., Li, S., Li, X., Chen, S., Novelli, A., Cho, C., Zeng, L., Wahner,
36 A., and Zhang, Y.: Winter photochemistry in Beijing: Observation and model simulation of OH
37 and HO₂ radicals at an urban site, *Science of The Total Environment*, 685, 85–95,
38 <https://doi.org/10.1016/j.scitotenv.2019.05.329>, 2019.

1 Ma, X., Tan, Z., Lu, K., Yang, X., Chen, X., Wang, H., Chen, S., Fang, X., Li, S., Li, X., Liu, J., Liu, Y.,
2 Lou, S., Qiu, W., Wang, H., Zeng, L., and Zhang, Y.: OH and HO₂ radical chemistry at a suburban
3 site during the EXPLORE-YRD campaign in 2018, *Atmospheric Chemistry and Physics*, 22,
4 7005–7028, <https://doi.org/10.5194/acp-22-7005-2022>, 2022.

5 Mallik, C., Tomsche, L., Bourtsoukidis, E., Crowley, J. N., Derstroff, B., Fischer, H., Hafermann,
6 S., Hüser, I., Javed, U., Keßel, S., Lelieveld, J., Martinez, M., Meusel, H., Novelli, A., Phillips, G. J.,
7 Pozzer, A., Reiffs, A., Sander, R., Taraborrelli, D., Sauvage, C., Schuladen, J., Su, H., Williams, J.,
8 and Harder, H.: Oxidation processes in the eastern Mediterranean atmosphere: evidence from
9 the modelling of HO_x measurements over Cyprus, *Atmospheric Chemistry and Physics*, 18,
10 10825–10847, <https://doi.org/10.5194/acp-18-10825-2018>, 2018.

11 Mao, J., Ren, X., Zhang, L., Van Duin, D. M., Cohen, R. C., Park, J.-H., Goldstein, A. H., Paulot,
12 F., Beaver, M. R., Crounse, J. D., Wennberg, P. O., DiGangi, J. P., Henry, S. B., Keutsch, F. N.,
13 Park, C., Schade, G. W., Wolfe, G. M., Thornton, J. A., and Brune, W. H.: Insights into hydroxyl
14 measurements and atmospheric oxidation in a California forest, *Atmos. Chem. Phys.*, 12,
15 8009–8020, <https://doi.org/10.5194/acp-12-8009-2012>, 2012.

16 Mauldin III, R. L., Kosciuch, E., Henry, B., Eisele, F. L., Shetter, R., Lefer, B., Chen, G., Davis, D.,
17 Huey, G., and Tanner, D.: Measurements of OH, HO₂+RO₂, H₂SO₄, and MSA at the South Pole
18 during ISCAT 2000, *Atmospheric Environment*, 38, 5423–5437,
19 <https://doi.org/10.1016/j.atmosenv.2004.06.031>, 2004.

20 Muller, J. B. A., Elste, T., Plass-Dülmer, C., Stange, G., Holla, R., Claude, A., Englert, J., Gilge, S.,
21 and Kubistin, D.: A novel semi-direct method to measure OH reactivity by chemical ionization
22 mass spectrometry (CIMS), *Atmos. Meas. Tech.*, 11, 4413–4433, [https://doi.org/10.5194/amt-](https://doi.org/10.5194/amt-11-4413-2018)
23 11-4413-2018, 2018.

24 Novelli, A., Hens, K., Tatum Ernest, C., Kubistin, D., Regelin, E., Elste, T., Plass-Dülmer, C.,
25 Martinez, M., Lelieveld, J., and Harder, H.: Characterisation of an inlet pre-injector laser-
26 induced fluorescence instrument for the measurement of atmospheric hydroxyl radicals,
27 *Atmos. Meas. Tech.*, 7, 3413–3430, <https://doi.org/10.5194/amt-7-3413-2014>, 2014.

28 Novelli, A., Vereecken, L., Bohn, B., Dorn, H.-P., Gkatzelis, G. I., Hofzumahaus, A., Holland, F.,
29 Reimer, D., Rohrer, F., Rosanka, S., Taraborrelli, D., Tillmann, R., Wegener, R., Yu, Z., Kiendler-
30 Scharr, A., Wahner, A., and Fuchs, H.: Importance of isomerization reactions for OH radical
31 regeneration from the photo-oxidation of isoprene investigated in the atmospheric
32 simulation chamber SAPHIR, *Atmos. Chem. Phys.*, 20, 3333–3355,
33 <https://doi.org/10.5194/acp-20-3333-2020>, 2020.

34 Sjostedt, S. J., Huey, L. G., Tanner, D. J., Peischl, J., Chen, G., Dibb, J. E., Lefer, B., Hutterli, M. A.,
35 Beyersdorf, A. J., Blake, N. J., Blake, D. R., Sueper, D., Ryerson, T., Burkhardt, J., and Stohl, A.:
36 Observations of hydroxyl and the sum of peroxy radicals at Summit, Greenland during
37 summer 2003, *Atmospheric Environment*, 41, 5122–5137,
38 <https://doi.org/10.1016/j.atmosenv.2006.06.065>, 2007.

1 Slater, E. J., Whalley, L. K., Woodward-Massey, R., Ye, C., Lee, J. D., Squires, F., Hopkins, J. R.,
2 Dunmore, R. E., Shaw, M., Hamilton, J. F., Lewis, A. C., Crilley, L. R., Kramer, L., Bloss, W., Vu, T.,
3 Sun, Y., Xu, W., Yue, S., Ren, L., Acton, W. J. F., Hewitt, C. N., Wang, X., Fu, P., and Heard, D. E.:
4 Elevated levels of OH observed in haze events during wintertime in central Beijing,
5 Atmospheric Chemistry and Physics, 20, 14847–14871, [https://doi.org/10.5194/acp-20-](https://doi.org/10.5194/acp-20-14847-2020)
6 14847-2020, 2020.

7 Stone, D., Whalley, L. K., and Heard, D. E.: Tropospheric OH and HO₂ radicals: field
8 measurements and model comparisons, Chem. Soc. Rev., 41, 6348,
9 <https://doi.org/10.1039/c2cs35140d>, 2012.

10 Tan, D., Faloon, I., Simpas, J. B., Brune, W., Shepson, P. B., Couch, T. L., Sumner, A. L., Carroll,
11 M. A., Thornberry, T., Apel, E., Riener, D., and Stockwell, W.: HO_x budgets in a deciduous forest:
12 Results from the PROPHET summer 1998 campaign, J. Geophys. Res., 106, 24407–24427,
13 <https://doi.org/10.1029/2001JD900016>, 2001.

14 Tan, Z., Fuchs, H., Lu, K., Hofzumahaus, A., Bohn, B., Broch, S., Dong, H., Gomm, S., Häseler, R.,
15 He, L., Holland, F., Li, X., Liu, Y., Lu, S., Rohrer, F., Shao, M., Wang, B., Wang, M., Wu, Y., Zeng,
16 L., Zhang, Y., Wahner, A., and Zhang, Y.: Radical chemistry at a rural site (Wangdu) in the
17 North China Plain: observation and model calculations of OH, HO₂ and RO₂ radicals,
18 Atmospheric Chemistry and Physics, 17, 663–690, <https://doi.org/10.5194/acp-17-663-2017>,
19 2017.

20 Tan, Z., Rohrer, F., Lu, K., Ma, X., Bohn, B., Broch, S., Dong, H., Fuchs, H., Gkatzelis, G. I.,
21 Hofzumahaus, A., Holland, F., Li, X., Liu, Y., Liu, Y., Novelli, A., Shao, M., Wang, H., Wu, Y., Zeng,
22 L., Hu, M., Kiendler-Scharr, A., Wahner, A., and Zhang, Y.: Wintertime photochemistry in
23 Beijing: observations of RO_x radical concentrations in the North China Plain during the BEST-
24 ONE campaign, Atmospheric Chemistry and Physics, 18, 12391–12411,
25 <https://doi.org/10.5194/acp-18-12391-2018>, 2018.

26 Tan, Z., Lu, K., Hofzumahaus, A., Fuchs, H., Bohn, B., Holland, F., Liu, Y., Rohrer, F., Shao, M.,
27 Sun, K., Wu, Y., Zeng, L., Zhang, Y., Zou, Q., Kiendler-Scharr, A., Wahner, A., and Zhang, Y.:
28 Experimental budgets of OH, HO₂, and RO₂ radicals and implications for ozone formation in
29 the Pearl River Delta in China 2014, Atmospheric Chemistry and Physics, 19, 7129–7150,
30 <https://doi.org/10.5194/acp-19-7129-2019>, 2019.

31 Tanner, D. J. and Eisele, F. L.: Present OH measurement limits and associated uncertainties, J.
32 Geophys. Res., 100, 2883, <https://doi.org/10.1029/94JD02609>, 1995.

33 Tanner, D. J., Jefferson, A., and Eisele, F. L.: Selected ion chemical ionization mass
34 spectrometric measurement of OH, J. Geophys. Res., 102, 6415–6425,
35 <https://doi.org/10.1029/96JD03919>, 1997.

36 Thames, A. B., Brune, W. H., Miller, D. O., Allen, H. M., Apel, E. C., Blake, D. R., Bui, T. P.,
37 Commane, R., Crounse, J. D., Daube, B. C., Diskin, G. S., DiGangi, J. P., Elkins, J. W., Hall, S. R.,
38 Hanisco, T. F., Hannun, R. A., Hints, E., Hornbrook, R. S., Kim, M. J., McKain, K., Moore, F. L.,

- 1 Nicely, J. M., Peischl, J., Ryerson, T. B., St. Clair, J. M., Sweeney, C., Teng, A., Thompson, C. R.,
2 Ullmann, K., Wennberg, P. O., and Wolfe, G. M.: Missing OH reactivity in the global marine
3 boundary layer, *Atmospheric Chemistry and Physics*, 20, 4013–4029,
4 <https://doi.org/10.5194/acp-20-4013-2020>, 2020.
- 5 Wang, M., Kong, W., Marten, R., He, X.-C., Chen, D., Pfeifer, J., Heitto, A., Kontkanen, J., Dada,
6 L., Kürten, A., Yli-Juuti, T., Manninen, H. E., Amanatidis, S., Amorim, A., Baalbaki, R., Baccarini,
7 A., Bell, D. M., Bertozzi, B., Bräkling, S., Brilke, S., Murillo, L. C., Chiu, R., Chu, B., De Menezes,
8 L.-P., Duplissy, J., Finkenzeller, H., Carracedo, L. G., Granzin, M., Guida, R., Hansel, A., Hofbauer,
9 V., Krechmer, J., Lehtipalo, K., Lamkaddam, H., Lampimäki, M., Lee, C. P., Makhmutov, V., Marie,
10 G., Mathot, S., Mauldin, R. L., Mentler, B., Müller, T., Onnela, A., Partoll, E., Petäjä, T., Philippov,
11 M., Pospisilova, V., Ranjithkumar, A., Rissanen, M., Rörup, B., Scholz, W., Shen, J., Simon, M.,
12 Sipilä, M., Steiner, G., Stolzenburg, D., Tham, Y. J., Tomé, A., Wagner, A. C., Wang, D. S., Wang,
13 Y., Weber, S. K., Winkler, P. M., Wlasits, P. J., Wu, Y., Xiao, M., Ye, Q., Zauner-Wieczorek, M.,
14 Zhou, X., Volkamer, R., Riipinen, I., Dommen, J., Curtius, J., Baltensperger, U., Kulmala, M.,
15 Worsnop, D. R., Kirkby, J., Seinfeld, J. H., El-Haddad, I., Flagan, R. C., and Donahue, N. M.:
16 Rapid growth of new atmospheric particles by nitric acid and ammonia condensation, *Nature*,
17 581, 184–189, <https://doi.org/10.1038/s41586-020-2270-4>, 2020.
- 18 Wang, X., Jacob, D. J., Eastham, S. D., Sulprizio, M. P., Zhu, L., Chen, Q., Alexander, B., Sherwen,
19 T., Evans, M. J., Lee, B. H., Haskins, J. D., Lopez-Hilfiker, F. D., Thornton, J. A., Huey, G. L., and
20 Liao, H.: The role of chlorine in global tropospheric chemistry, *Atmospheric Chemistry and
21 Physics*, 19, 3981–4003, <https://doi.org/10.5194/acp-19-3981-2019>, 2019.
- 22 Wennberg, P. O., Bates, K. H., Crounse, J. D., Dodson, L. G., McVay, R. C., Mertens, L. A., Nguyen,
23 T. B., Praske, E., Schwantes, R. H., Smarte, M. D., St. Clair, J. M., Teng, A. P., Zhang, X., and
24 Seinfeld, J. H.: Gas-Phase Reactions of Isoprene and Its Major Oxidation Products, *Chem. Rev.*,
25 118, 3337–3390, <https://doi.org/10.1021/acs.chemrev.7b00439>, 2018.
- 26 Whalley, L. K., Edwards, P. M., Furneaux, K. L., Goddard, A., Ingham, T., Evans, M. J., Stone, D.,
27 Hopkins, J. R., Jones, C. E., Karunaharan, A., Lee, J. D., Lewis, A. C., Monks, P. S., Moller, S. J.,
28 and Heard, D. E.: Quantifying the magnitude of a missing hydroxyl radical source in a tropical
29 rainforest, *Atmos. Chem. Phys.*, 11, 7223–7233, <https://doi.org/10.5194/acp-11-7223-2011>,
30 2011.
- 31 Whalley, L. K., Blitz, M. A., Desservettaz, M., Seakins, P. W., and Heard, D. E.: Reporting the
32 sensitivity of laser-induced fluorescence instruments used for HO₂ detection to an
33 interference from RO₂ radicals and introducing a novel approach that enables HO₂ and certain
34 RO₂ types to be selectively measured, *Atmospheric Measurement Techniques*, 6, 3425–3440,
35 <https://doi.org/10.5194/amt-6-3425-2013>, 2013.
- 36 Wolfe, G. M., Marvin, M. R., Roberts, S. J., Travis, K. R., and Liao, J.: The Framework for 0-D
37 Atmospheric Modeling (F0AM) v3.1, *Geosci. Model Dev.*, 9, 3309–3319,
38 <https://doi.org/10.5194/gmd-9-3309-2016>, 2016.
- 39 Woodward-Massey, R., Slater, E. J., Alen, J., Ingham, T., Cryer, D. R., Stimpson, L. M., Ye, C.,

- 1 Seakins, P. W., Whalley, L. K., and Heard, D. E.: Implementation of a chemical background
2 method for atmospheric OH measurements by laser-induced fluorescence: characterisation
3 and observations from the UK and China, *Atmospheric Measurement Techniques*, 13, 3119–
4 3146, <https://doi.org/10.5194/amt-13-3119-2020>, 2020.
- 5 Xu, Z., Xue, L., Wang, T., Xia, T., Gao, Y., Louie, P. K. K., and Luk, C. W. Y.: Measurements of
6 Peroxyacetyl Nitrate at a Background Site in the Pearl River Delta Region: Production
7 Efficiency and Regional Transport, *Aerosol Air Qual. Res.*, 15, 833–841,
8 <https://doi.org/10.4209/aaqr.2014.11.0275>, 2015.
- 9 Yang, X., Lu, K., Ma, X., Liu, Y., Wang, H., Hu, R., Li, X., Lou, S., Chen, S., Dong, H., Wang, F.,
10 Wang, Y., Zhang, G., Li, S., Yang, S., Yang, Y., Kuang, C., Tan, Z., Chen, X., Qiu, P., Zeng, L., Xie,
11 P., and Zhang, Y.: Observations and modeling of OH and HO₂ radicals in Chengdu, China in
12 summer 2019, *Science of The Total Environment*, 772, 144829,
13 <https://doi.org/10.1016/j.scitotenv.2020.144829>, 2021.
- 14 Yang, X., Lu, K., Ma, X., Gao, Y., Tan, Z., Wang, H., Chen, X., Li, X., Huang, X., He, L., Tang, M.,
15 Zhu, B., Chen, S., Dong, H., Zeng, L., and Zhang, Y.: Radical chemistry in the Pearl River Delta:
16 observations and modeling of OH and HO₂ radicals in Shenzhen in 2018, *Atmospheric
17 Chemistry and Physics*, 22, 12525–12542, <https://doi.org/10.5194/acp-22-12525-2022>, 2022.
- 18 Yang, Y., Shao, M., Wang, X., Nölscher, A. C., Kessel, S., Guenther, A., and Williams, J.: Towards
19 a quantitative understanding of total OH reactivity: A review, *Atmospheric Environment*, 134,
20 147–161, <https://doi.org/10.1016/j.atmosenv.2016.03.010>, 2016.
- 21 Zou, Z., Chen, Q., Xia, M., Yuan, Q., Chen, Y., Wang, Y., Xiong, E., Wang, Z., and Wang, T.: OH
22 measurements in the coastal atmosphere of South China: possible missing OH sinks in aged
23 air masses, *Atmospheric Chemistry and Physics*, 23, 7057–7074, [https://doi.org/10.5194/acp-
24 23-7057-2023](https://doi.org/10.5194/acp-23-7057-2023), 2023.

25